REVIEW OF BASICS MATERIAL CHARACTERISATION OF II-VI THIN FILM SEMICONDUCTORS FOR USE IN SOLAR CELL FABRICATION

D. G. Diso[1] and A. O. Musa[2]

[1]*Department of Physics, Kano University of Science & Technology, Wudil, PMB 3244, Kano-Nigeria.*
[2]*Department of Physics, Bayero University Kano, PMB 3011, Kano-Nigeria.*
E-mail: dgdiso@yahoo.co.uk

ABSTRACT

Thin film semiconductors based on group II-VI family have been widely studied due to the need to maximize the electrical and optical properties of these materials for use as solar cells. A wide range of analytical techniques are normally used to investigate the layers of these materials. Some of the basic techniques used to characterise the deposited films include photo electrochemical (PEC) studies, optical absorption, X-ray diffraction (XRD), X-ray fluorescence (XRF), scanning electron microscopy (SEM), atomic force microscopy (AFM), Raman spectroscopy and X-ray photoelectron spectroscopy (XPS). This paper reviews in details these techniques and combines relevant results from the literature with more emphasis on CdTe, CdS and ZnTe in which the main author work with.

Keywords: Material Characterisation, CdTe, CdS, ZnTe, Thin Films

INTRODUCTION

Material characterisation is necessary before working with any semiconductor materials. It is very easy to identify any semiconductor material during the growth process by the appearance (colour). From the literature, it is known that ZnTe is reddish-brown (Diso *et al.*, 2011), CdS is yellow (Diso *et al.*, 2010) and CdTe is black (Dharmadasa *et al.*, 2002). To confirm this, other analytical techniques must be tested. PEC measurements were used to identify the electrical conductivity type of all the semiconductor layers. Hall Effect or thermo-electric effect is usually used for this purpose, but both techniques are not possible with glass/TCO/material layers due to the underlying conductor (TCO layer). Optical properties are measured using a Cary 50 Scan UV-Visible spectrometer (Varian Australia Pty. Ltd). X-ray diffraction measurement are carried out using an X'Pert Pro diffractometer (Philips Analytical, Almelo, The Netherlands) with CuK_α excitation ($\lambda = 1.5416$ Å) for structural analysis of the deposited film. Morphology of the surfaces are observed using the Scanning Electron Microscopy (SEM) and Atomic Force Microscopy (AFM). The SEM images

are normally taken using FEG NOVA NANO SEM equipment (FEI Company, Holland), while JSMP-5200 system (JEOL, Tokyo, Japan) are used for AFM measurement. A detector attached to the SEM equipment can be used to investigate the chemical composition using a technique called Energy Dispersive Analysis of X-rays (EDAX). Another technique can also used for this purpose with more emphasis on the atomic percentage of the constituents elements under lying the films called XRF using a Philips Magix PRO PW 2440 sequential x-ray fluorescent spectrometer. Raman spectra of the samples are usually recorded using a Raman spectrometer (RENISHAW InVia Raman Microscope, Hoffman Estates, IL, USA) with Ar^+ laser having wavelength 514 nm and 15 mW as the power source. The XPS studies can be performed using an Escalab 250 spectrometer with a monochromatized Al anode x-ray source (hv = 1486.6 eV). The binding energies obtained from the XPS analysis can be standardized for specimen charging using C 1s as the reference at 284.5 eV.

MATERIALS CHARACTERISATION

This section discusses the basic theory from the relevant books and journals from the literature. It also describes how each technique is used to analyse the material layers under consideration. Typical results that go with each technique from the authors work are also highlighted and included in this review.

Photoelectrochemical (PEC) cell

The conductivity type of a semiconductor can be determined using a PEC cell measurement. Working and counter electrodes are connected to a potentiometer and placed in a suitable electrolyte to form a solid/liquid junction. Once connected, the voltages between the two electrodes are measured both in the dark and under illumination. The difference between these two voltage values gives the open circuit voltage of the liquid/solid junction or the PEC signal. The sign of the PEC signal determines the conductivity type of the semiconducting layer, and the magnitude of the signal indicates the doping concentration. A zero PEC signal is produced for both metallic and insulating layers and the largest PEC signal is produced by semiconductor with optimum doping. Figures 1 (a) and (b) show the band diagrams of n-type and p-type semiconductor/liquid junctions respectively. For n-type semiconductor, the holes move towards the surface of the semiconductor and the electrons move into the bulk of the material. In the case of a p-type semiconductor electron flow is opposite to that of a n-type semiconductor system. An extreme care should be taken when using PEC measurement because the results can be affected by surface oxidation and Fermi level pinning. The system can be calibrated using a well known material (e.g. CdS) which is n-type as grown (Dharmadasa *et al.*, 2002).
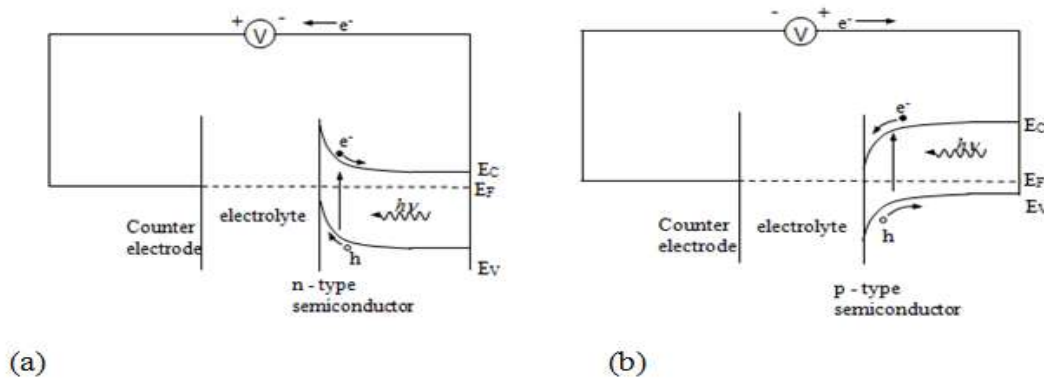
Figure 1: Band diagrams of solid/liquid junction for (a) n-type and (b) p-type semiconductors (Tolan, 2008).

A typical PEC cell signal of glass/FTO/CdTe layers grown at different cathodic voltages is shown in Figure 2. From the Figure, at lower cathodic voltages the polarity of the PEC signal indicate p-type shows Te-rich surface because Te has a more positive E^o value of +0.593 V. Similarly, when the cathodic voltages are higher the PEC signal will indicate n- type conductivity indicating Cd-rich surface with an E^o value of -0.403 V (Martin, 2010). At deposition voltage of 1.576 V, the PEC signal shows intrinsic (i.e. stoichiometric) with Cd:Te = 50:50. At this point the intrinsic carrier concentration is of the order of n = p~10^{10}cm^{-3} which indicates that the position of the Fermi level should be in the middle of the band-gap. The PEC signal arises because of the formation of Photovoltaic active depletion region as a result of moderate doping ~$(10^{14} - 10^{17})$ cm^{-3}. These results confirmed the work of other researchers who reported the possibility of getting either p- or n- type CdTe (Dharmadasa *et al.*, 1989; Yang *et al.*, 2010; Oktik, 1989).
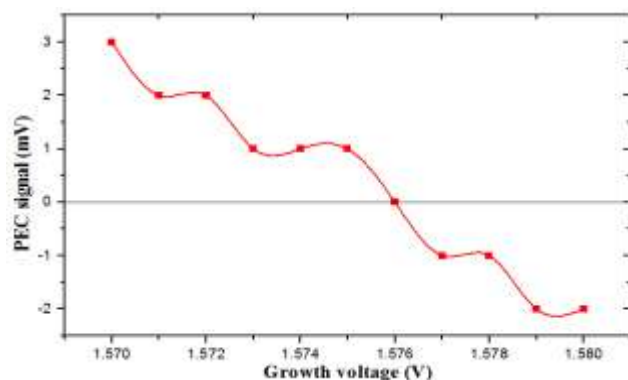

Figure 2: PEC signal as a function of growth voltage for glass/FTO/CdTe layers.

Optical Absorption

Optical absorption measurements were carried out to evaluate the bandgap of the semiconducting materials. The value of the bandgap indicates how the semiconducting

layers perform as absorbers of light. The absorption coefficient, α is a function of the wavelength of the light. The bandgap energy, E_g values can be derived from mathematical treatment of data obtained from optical absorbance versus wavelength with the Stern relationship (Sze and Kwok, 2007) of near absorption edge data using;

$$\alpha = \frac{k\left(hv - E_g\right)^{\frac{n}{2}}}{hv}$$
(1)

where, v is the frequency, h is Planck's constant, and n carries the value of either 1 or 4, (the value of n is 1 and 4 for direct and indirect transitions respectively).

Equation (1) shows that α increases sharply as the energy of photons exceeds E_g, so that a well-defined absorption edge is expected in semiconductor materials with a direct bandgap. To obtain transmission spectra, the same instrument is used with the transmission data mode selected from the menu of the instrument. The bandgap energy of the semiconductor determines the percentage transmission of light of known wavelength through the material. Figure 3 shows the main features of the spectrophotometer. It consists of four main components: (i) the light source which produces the required region of the spectrum, (ii) the monochromator which receives the input from the light source and outputs is tuneable highly monochromatic light, (iii) the sample chamber where the sample to be analysed is placed, and (iv) the detector (www.wellesley, 2015).
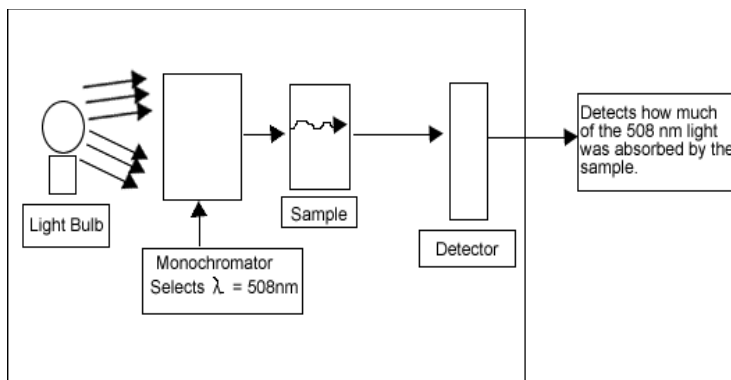

Figure 3: The main features of a spectrophotometer.

Other parameters that can be analysed from this technique includes absorption coefficient, refractive index, extinction coefficient etc.

Absorption coefficient: This is defined as the decrease in the intensity of beam of photons on particles in its passage through a medium. When a radiation of intensity I_o is incident on a

material of thickness d and the transmitted intensity I_t is obtained by the expression (Kittle, 1996);

$$\frac{I_t}{I_o} = \exp(-\alpha d)$$

(2)

Similarly, the transmittance T can be obtained using equation (3) as;

$$A = -\log_{10} T, \Rightarrow T = 10^{-A}$$

(3)

Refractive index (n): It plays an important role in the search for optical materials, being a significant factor in optical communication and in designing devices for spectral dispersion. The refractive index determines the propagation velocity of photons in the material. The value of n was calculated using the relation (Kittle, 1996):

$$R = \frac{(n-1)^2}{(n+1)^2}$$

(4)

where R is the normal reflectance.

Extinction coefficient (k): The extinction coefficient is a measure of the rate of the reduction of transmitted light through a substance. The extinction coefficient, k of the thin films is also calculated using the formula (Kittle, 1996):

$$k = \frac{\alpha \lambda}{4\pi}$$

(5)

where λ is the wavelength of light.

A typical graph of optical absorption for CdS films deposited at different growth voltages is shown in Figure 4 (Aliyu *et al*, 2013). The values of the E_g were determined by plotting the square of absorption (A^2) against photon energy ($h\nu$) using equation 1. The straight-line portion is extrapolated to cut the photon energy axis, which gives the energy bandgap.
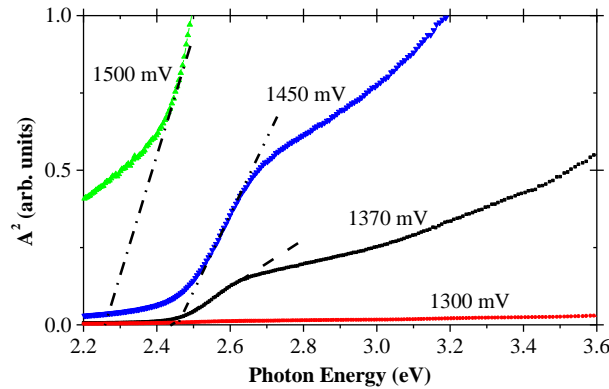
Figure 4:   Optical absorption curves for CdS deposited at different growth voltages.

From the Figure, it can be seen that the direct bandgap of the sample deposited at growth voltage 1450 mV has a bandgap of 2.44 eV which is very close to the theoretical value of CdS thin films reported by other researchers (Izgorodi *et al.*, 2009; Dharmadasa *et al.*, 1996).

Similarly, the variation of the refractive index of the CdS films at various growth voltages is shown in Figure 5. The Figure shows that at the wavelength of 512 nm, the refractive index, *n* of the film decreased from 0.70 to 0.03 with increasing growth voltage from 1300 to 1500 mV. It was reported from the literature (Kariper *et al.*, 2012; Patil and Pawar, 2012) that, the decrease in the refractive index is associated with the fundamental bandgap absorption. The reduction of *n* is very important because it determines the propagation speed of light in the material medium according to the relation $n = \frac{c}{v^2}$. A decrease in *n* means an increase in the velocity at which light propagate in the material layer.
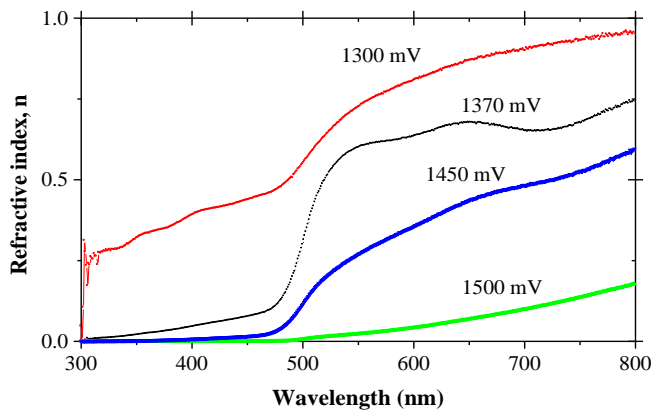

Figure 5: The dependence of the refractive index on wavelength as a function of the growth voltage.

X-ray diffraction (XRD)

XRD is used to identify the structure and phases of a material and is a non-destructive technique. Other uses include determination of texture and residual stress in films. Wilhelm Roentgen in 1895 (Cullity and Stock, 2001) while he was experimenting with a Crookes tube discovered X-rays. The scattering centres for x-rays rely on the fact that crystals are composed of regularly spaced atoms. X-ray waves interact with the atoms in a crystal as shown in Figure 6, in such a way as to produce interference. Diffraction will occur if the wavelength of the x-ray and the atomic spacing of the crystal are comparable.
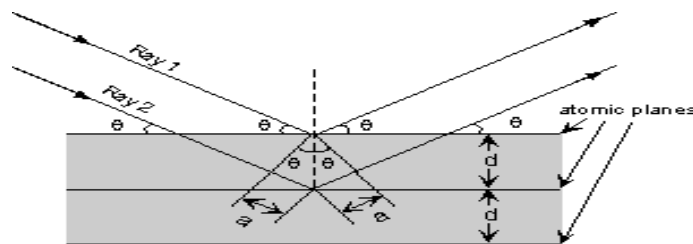

Figure 6: X-ray diffraction beam through a parallel section of crystal lattice (http://Serc, 2015).

Let θ be the angle which the x-rays enters a crystal with one of these atomic planes and $2a$ be the path difference between two rays. For constructive interference to occur (http://Serc, 2015);

$$2a = n\lambda \tag{6}$$

From Figure 6,

$$a = d \sin\theta, \qquad \therefore 2d \sin\theta = n\lambda \tag{7}$$

Where, n is an integer, λ is the wavelength of x-rays incident on a crystal and d is the distance between lattice planes. Equation (6) is known as Bragg's Law for x-ray diffraction.

A strong diffracted beam occurs if the rays scattered by all the atoms in the planes interfere constructively and are in phase. Furthermore, constructive interference would fail if the scattering atoms are not arranged in a regular periodic manner and the scattered rays would have random phase. In a Bragg Brentano diffractometer, the x-ray intensity is measured by a scintillation counter which is mounted to a measuring device called a goniometer at an angle. The sample and the counter are both rotated (but the rotation of the counter is on the diffractometer circle). A practical XRD instrument comprises three main elements; an x-ray source, a prepared sample and a detector as shown in Figure 7.
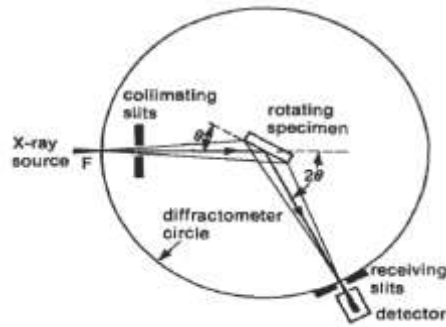
Figure 7: Configuration of glancing angle diffractometer (Brundle, 1992).

All XRD spectra are presented in a log-linear form in which the horizontal 2θ axis has a linear scale and the vertical (count) axis uses a log scale. The diffraction peaks are analysed using equation (7) to determine the d_{hkl} spacing of the plane causing that peak. The characteristics of the unit cells of each phase present in the material can be determined from the intensity and position of the peaks. The material can be identified by comparing peak positions with standard data files called Joint Committee on Powder Diffraction Standard (JCPDS). From the full width at half maximum (FWHM), the strain, grain size and lattice parameters can be calculated as follows:

The Scherer equation is used to calculate the grain size, D (Cullity and Stock, 2001);

$$D = \frac{k\lambda}{\beta \cos\theta} \qquad (8)$$

where, β is the full width at half maximum of the peak corrected for instrumental broadening, λ is the wavelength of the x-rays, θ is the Bragg angle and k is the Scherer constant taken to be 0.94.

The Hull equation is used to calculate the strain (ε) and is given by (Cullity and Stock, 2001);

$$\beta \cos\theta = \varepsilon \sin\theta + \frac{\lambda}{D} \qquad (9)$$

The lattice parameters for a hexagonal crystal can be calculated using equation 10 (Cullity and Stock, 2001);

$$\frac{1}{d^2} = \frac{h^2 + k^2}{a^2} + \frac{l^2}{c^2} \qquad (10)$$

Figure 8 shows a typical X-ray diffraction patterns for as deposited and heat treated CdTe layers (at 450°C for 15 minutes) deposited at three different growth voltages (Diso, 2011).

The main diffraction peak at $2\theta = 23.642^o$ which corresponds to preferred orientation along (111) plane of cubic phase. This peak agrees with the JCPDS (01-075-2086) data of cubic CdTe. From these Figures, it is observed that at lower growth voltage (panel 1: $V_g = 1.563$ V), Te is deposited more than Cd on the substrate surface, giving rise to Te-rich CdTe material. As the deposition potential increases, the Te peaks in the diffractograms diminish, at 1.574 V and above, only one peak ascribed to $CdTeO_3$ is seen. At higher growth voltages (panel 8: $V_g = 1.587$ V), more Cd than Te are deposited on the substrate surface and the resulting films produced are Cd-rich CdTe material. Weak Cd peaks were also observed as expected in this diffractogram. At the intrinsic composition 1.576 eV, the CdTe (111) peak is dominant and all other peaks diminished as shown in panel 5. As shown from the PEC result in section 2.1, this material is i-type in electrical conductivity which is similar to the results earlier reported (Yang *et al.*, 2009).
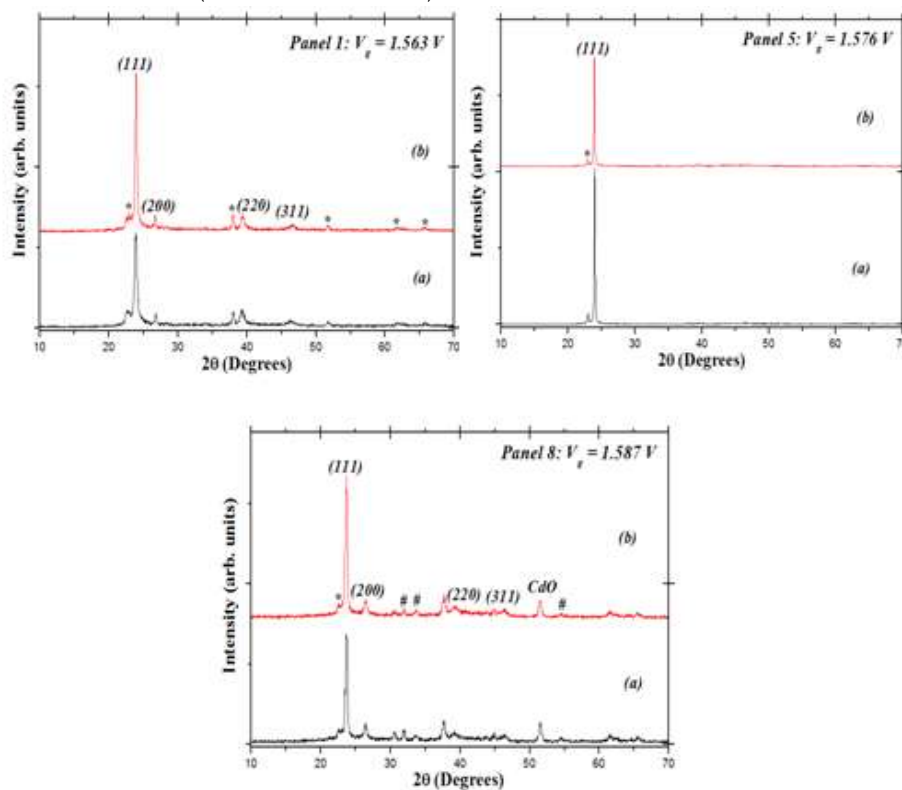

Figure 8:   X-ray diffraction patterns for CdTe layers at different growth voltages (a) as deposited and (b) heat treated [•and #indicates Te and Cd related peaks respectively].

After heat treatment in air, the intensity of the peaks was different. At lower and higher growth voltages, the intensity goes up as a result of the films becoming more crystalline. At the intrinsic potential and the potential which are very close to the stoichiometry, the intensity goes down due to loss of the material through sublimation. The heat treatment

enhances the recrystallisation of non–stoichiometric CdTe films reducing any stress within the films and due to sublimation of excess elements from the layers.

Scanning Electron Microscopy (SEM)

SEM studies can be carried out to investigate the surface morphology, grain size and orientation of materials making up the sample. Figure 9 shows the schematic diagram of a typical SEM. An electron gun is used to generate a monochromatic electron beam which passes through the first condenser lens with condenser aperture attached. The aperture is used to eliminate some high angle electrons. A focussed beam is now generated by fine focussing using a second condenser lens. A grid pattern is now produced by the deflection coils and scanned onto the desired area of the sample by the final lens. A vacuum is required in order to avoid scattering and absorption. Several interactions take place when the electron beam is focused on the sample surface and what is emitted from the surface is detected by a suitable detector. Chemical information about the sample may be obtained from the characteristics x–rays emitted from the specimen. An energy dispersive x–ray (EDX) spectrometer consists of a solid state x–ray detector mounted within the SEM chamber. It is usually made from lithium–drifted silicon, Si(Li); and signal processing electronics. An x–ray energy histogram is displayed as a result of the signal conversion by the Si(Li) detector after the emitted x–rays are detected. A series of peaks representative of each element displayed with their relative amount and the atomic composition of the element can be estimated (Egerton, 2005).
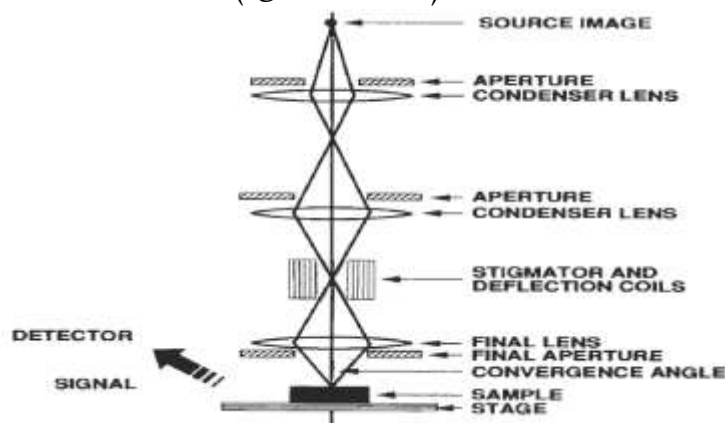

Figure 9: A schematic diagram of SEM (Brundle, 1992).

Secondary electron micrographs of a typical as deposited and heat treated CdS samples grown at 1500 mV are shown in Figure 10 (Diso, 2011). The material clusters are in the nanoscale range with an average size of ~60 nm. These grains seem to be isolated from each other with gaps in between, and there is no apparent change in morphology or material cluster size observed after heat treatment. From the Figure, the SEM images show

gaps or pin holes between the grains which indicates the growth of CdS as islands. Therefore, it is possible during CdTe growth; some CdTe layers grow on the FTO while others are on the CdS film. This creates some gaps or pin holes and when contacts are made with Au for complete devices it will provide shorting paths making devices low in efficiency.
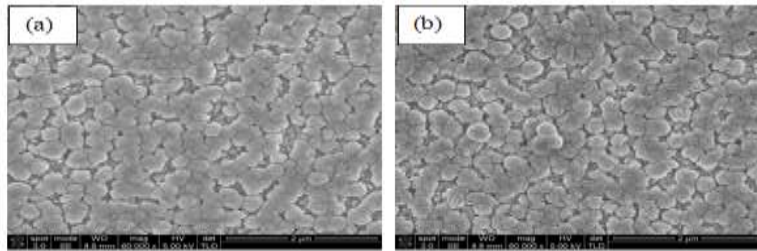
Figure 10.SEM images of ED-CdS grown at 1500 mV on glass/FTO substrate (a) as deposited and (b) heat treated.

Atomic Force Microscopy (AFM)

This technique developed in 1986 (Hubbard, 1995) and resolve images down to a single atom and has a huge advantage over electron and conventional optical microscopes. It gives 2D & 3D-images and can give a true topographic view of the sample with its vertical view. Figure 11 shows a schematic diagram of a typical AFM instrument. A micro fabricated cantilever is used as the probe which forces sensors placed on the sharp tip that is positioned on or below the sample surface. Generally, the piezoelectric actuator which is under computer control moves the sample very precisely while the tip is stationary. AFM can be operated in three modes which includes contact mode (true), non-contact mode and intermittent (called tapping) mode.

- Contact mode: Soft silicon nitride cantilever is typically used to probe the surface. The tip is kept at a fixed height at or above the surface and the cantilever deflection is used to generate an image.
- Non-contact mode: The tip is oscillated at its resonant frequency at some small distance above the surface. The signal applied to the piezoelectric actuators needed to keep the resonant frequency constant is then used to generate a topographic image.
- Intermittent mode: The cantilever is initially oscillated at its resonance frequency at amplitudes much greater than those utilized in non-contact mode. The tip comes in contact with the surface as it is brought close to the surface and its amplitude is

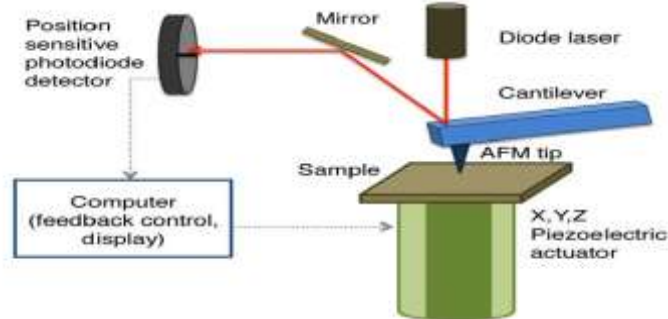reduced. This is the preferred method of imaging when atomic resolution is not needed (Martin, 2010).

Figure 11: Schematic diagram of a typical AFM instrument (Martin, 2010).

A typical 2D-AFM picture for heat treated CdTe layers grown at 1.576 V is shown in Figure 12 (Diso, 2011). From the Figure it is observed the AFM image show a cluster of CdTe with large grains. The material clusters are in micro-scale range with an average size of ~1.2 μm. These grains seem to be well-connected to each other.
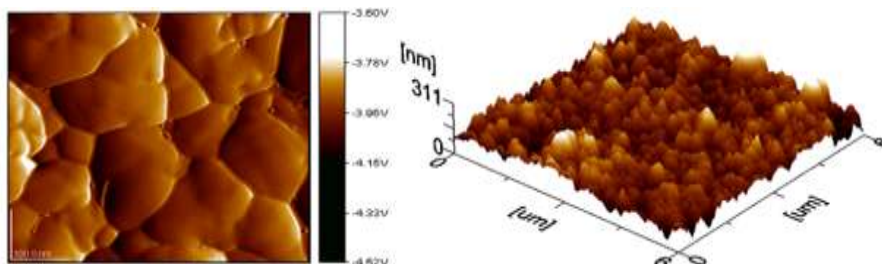
Figure 12: 2D-AFM images for heat treated CdTe layers grown at 1.576 V.

A typical 3D-AFM picture of ED-CdS is also shown in Figure 13. It can be observed from the Figure that CdS fabricated have highly ordered and densely packed nano-rod arrays oriented perpendicular to the glass/FTO substrates and grow upwards after nucleation on the FTO surface. There are many empty spaces between nano-rods; these observations are consistent with the SEM results shown in Figure 10. The 3D-AFM reveals the existence of tightly packed nano-rods with length equal to ~70 nm (thickness of the CdS layer) and diameter of ~40 nm. The presence of nano-rods provides advantages because of band bending due to enhanced surfaces and hence creating an additional internal electric field perpendicular to their axis. It also minimises recombination of electrons and holes in which the electrons flow along the axis of the nano-rod and holes could flow in the opposite direction along the vicinity of the surface layer of the nano-rod.
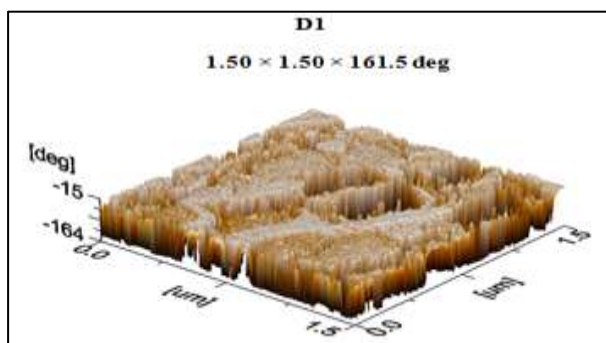
Figure 13: A 3D-AFM image of ED-CdS grown at 1500 mV on glass/FTO substrate.

X-ray Fluorescence (XRF)

This technique involves excitation by high energy x-ray or gamma ray bombardment of materials, thereby creating the emission of characteristic secondary (or fluorescent) x-rays from it. It is a destructive technique and gives the atomic percentage of the individual elements in the material. Figure 14 shows a schematic diagram of XRF spectrometer. When the x-rays strike the sample, diffraction occurs which is later send through focusing slit to analysing crystal. Photons are diffracted with various wavelengths from the analysing crystal and collected by the detector which transfers them to the computer for analysis.
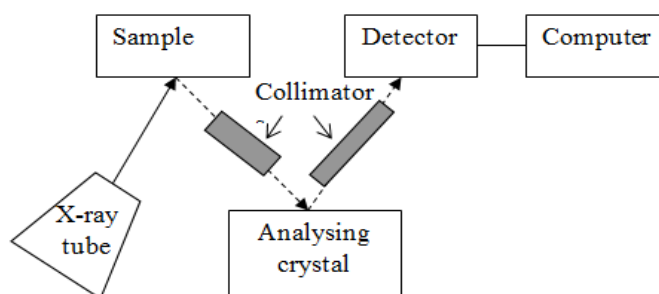

Figure 14: A schematic diagram of XRF spectrometer (Salaoru, 2006).

The stoichiometry of the ED-CdS layers was investigated using XRF in order to correlate the material and atomic percentages of individual elements. Figure 15 shows the typical XRF analysis for both as deposited and heat treated CdS layers. From the Figure, at low cathodic voltages, S deposits preferentially and Cd deposition increases as the cathodic voltage is increased. At voltages close to 1590 mV, the material becomes stoichiometric, reaching 50 atom% for both materials.
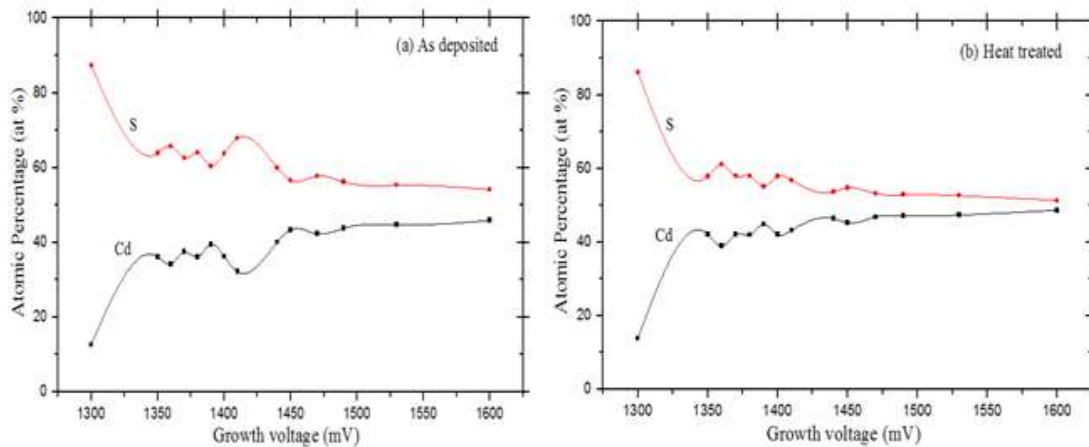
Figure 15: XRF analysis showing the atomic percentages of Cd and S for (a) as deposited and (b) heat treated ED-CdS layers grown on glass/FTO substrates.

Raman Spectroscopy

Raman spectroscopy is a technique used to identify and provide information on chemical structures and physical forms from the characteristic spectral pattern (finger prints) of the material. In 1928, Raman and Krishnan first experimentally observed the phenomenon of inelastic scattering of light after it was postulated by Smekal in 1923. Later on, this phenomenon was named as Raman spectroscopy. Raman spectroscopy relies on inelastic scattering of monochromatic light, usually from a laser in the visible, near IR or near UV range. Light interacts with phonons or other excitation in the system and as a result the incident photon's energy shifts up or down. Figure 16 shows the schematic diagram of a Raman spectrometer instrument. A Laser is focussed through a pinhole and then collected as an expanded parallel beam. The beam is used to collect the laser focused through a pinhole. A notch filter is used for the radiation which serves as interference filters. The charged coupled device (CCD) detector detects the light after passing into a monochromator. The wave number scale for most vibrations extends from 50 cm^{-1} to about 1800 cm^{-1} with some molecular vibrations extending to 3500 cm^{-1}. Line widths are on the order of 1-5 cm^{-1}.
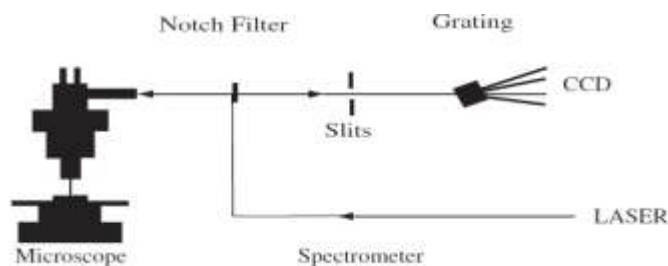

Figure 16: A schematic diagram of a Raman spectrometer instrument (Smith and Dent, 2005).

The Raman spectrum of ZnTe epilayer grown on GaAs substrate is shown in Figure 17 for comparison (Wiedemeier, 2011). Figure 18 shows the typical Raman spectrum of electrodeposited ZnTe layer grown on glass/FTO substrate at 1513 mV. Two peaks were observed at 203 cm^{-1} and 409 cm^{-1} which correspond to the first and second order longitudinal optical phonons (1LO) and (2LO) of ZnTe respectively. All these peaks are very close to those found by other researchers (Ersching*et al.,*, 2009; Oh *et al.,* 1993). A similar observation of these two peaks has been reported (Szuszkiewicz *et al.,* 2009). They also reported that the group of lines observed between 90 cm^{-1} and 150 cm^{-1} (i.e. Te labelled) is due to Raman scattering at trigonal tellurium clusters. Furthermore, the LO phonon line intensity has a clear maximum for an excitation energy of 2.34 eV, close to the excitation energy of ZnTe. A Raman spectrum shows that electrodeposited ZnTe films is Te-rich with a strong Te- peak observed. This indicates that the deposited film is Te-rich surface. Therefore, stoichiometric ZnTe must be produced which is necessary for good devices.
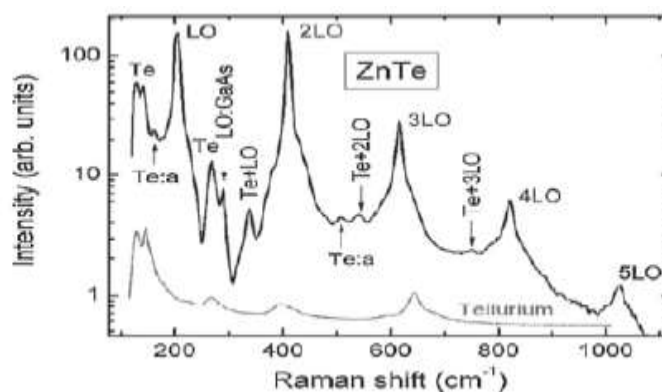

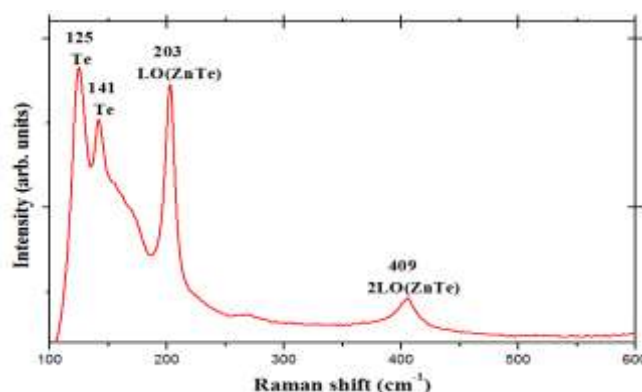Figure 17: Raman spectra of ZnTe epilayer grown on GaAs substrate (Wiedemeier, 2011).

Figure 18: Raman spectrum of electrodeposited ZnTe grown on glass/FTO substrate at 1513 mV.

X-ray Photoelectron Spectroscopy (XPS)

The XPS technique uses single energy x-ray photons as a source of irradiation to the sample and detects the photoelectrons emitted from the surface. The photoelectric effect is the basic principle of XPS, was first discovered by Hertz, and later K. Siegbahn extended it to surface analysis (Briggs and Seah, 1990; Siegbahn, 1965). The technique is also useful for quantitative analysis of surface composition. The binding energies of all elements can be detected except hydrogen and helium. The kinetic energy of the x-ray photons used ranges from 300 to 1500 eV. Due to the short range of the x-ray photons, inelastic scattering is absent during electron travelling. Figure 19 shows the schematic diagram of photoemission process used for XPS. An electron is emitted from the surface of the sample when a photon is absorbed. The kinetic energy of the emitted electron is (Moulder, 1995);

$$KE = h\nu - BE - \varphi_s \tag{11}$$

where, $h\nu$ is the characteristics energy of the x-ray photon, BE is the binding energy of the core level electron and φ_s is the work function of the spectrometer.

Spectral lines or photoelectron peaks as a function of binding energy appear due to the electrons emitted from the sample without loss of inelastic energy. A spectral background also appears as a result of energy lost by the electrons. This binding energy of the ejected electrons is (Moulder, 1995);

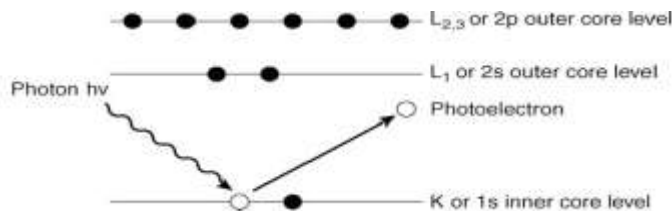$$BE = h\nu - KE - \varphi_s \tag{12}$$

Figure 19: A schematic diagram of photoemission process used in XPS (Martin, 2010).

Two different modes are used to collect the XPS data:

- Wide scans or survey spectra are used to get more information about the true nature of the surface composition. A wide energy range, typically ~1000 eV, is employed.
- Narrow scans with smaller energy windows are used at higher energy resolution to determine the chemical state of a specific element.

The XPS spectrum of vacuum cleaved CdS is shown in Figure 20 together with a typical spectrum obtained for an electrodeposited CdS layer grown at 1500 mV in Figure 21 for comparison.
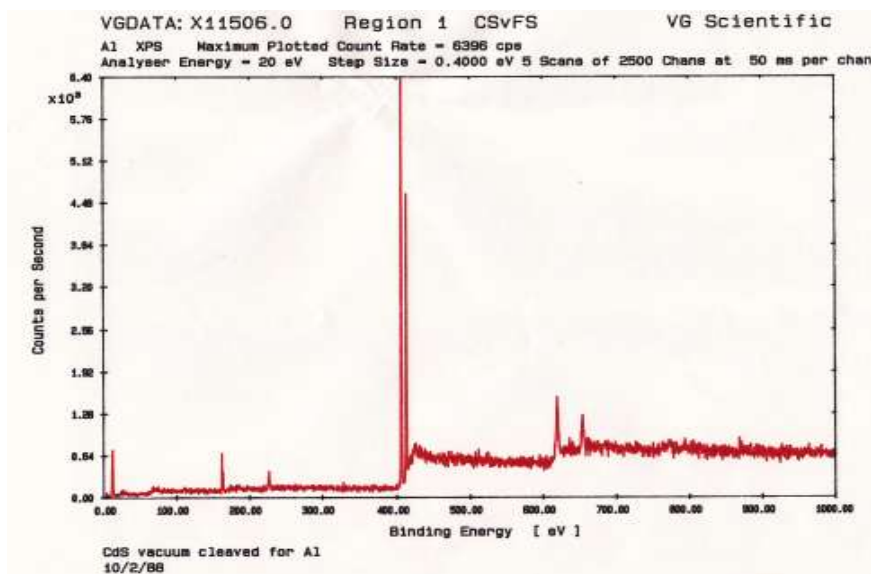

Figure 20: XPS spectrum of CdS cleaved in vacuum (courtesy: I. M. Dharmadasa).
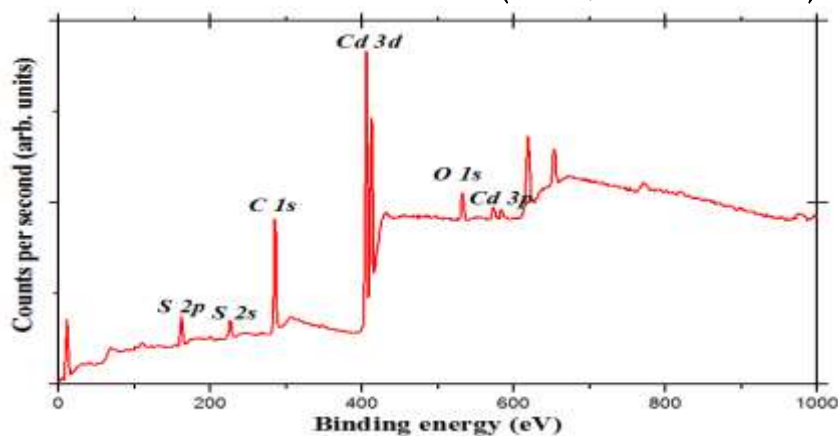

Figure 21: A typical XPS survey spectrum of the electrodeposited CdS pattern grown at 1500 mV.

The two XPS spectra reveals that electrodeposited CdS have similar spectrum to that of a clean cleaved CdS except for the additional presence of carbon (C) and oxygen (O) peaks which may be due to surface contamination. From Figure 21, two distinct Cd 3d peaks (i.e. $3d_{5/2}$ and $3d_{3/2}$) are observed and presented more clearly in Figure 22. The binding energies associated with Cd ($3d_{5/2}$ and $3d_{3/2}$) appeared at ~405.6 and ~412.3 eV respectively. Similarly, Figure 23 shows the S 2p peak and has a binding energy of ~162.5 eV. The atomic ratio for Cd:S given from the XPS spectra is 52.9:47.1. This experimental result

confirmed the XRF measurements discussed under section 2.6. All these peaks and binding energies are very close to those found by other researchers and summarised in Table 1 (Dharmadasa *et al.*, 1989; Mazōn–Montijo *et al.*, 2010; Vemuri *et al.*, 2010; Karimi *et al.*, 2009).
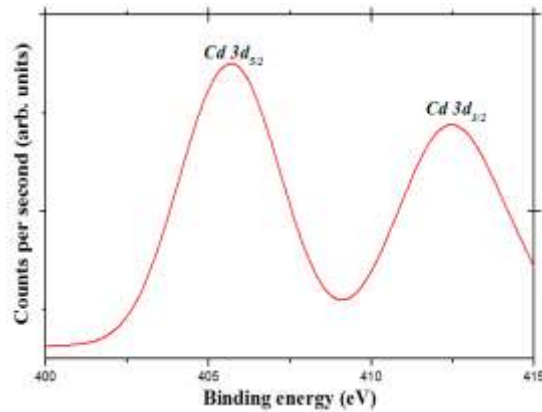

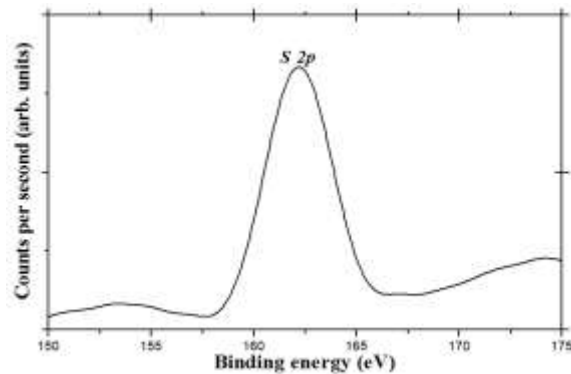Figure 22: XPS spectrum of electrodeposited CdS grown at 1500 mV close–up survey for Cd 3d core.

Figure 23: XPS spectrum of electrodeposited CdS grown at 1500 mV close–up survey for S 2p core.

Table 1: Summary of CdS XPS results

Method	Binding energy (eV)			Ref.
	Cd 3d$_{5/2}$	Cd 3d$_{3/2}$	S 2p	
CBD	405.5	412	161.70	Karimi *et al.*, 2009
ammonia–free chemical process	405.1 – 405.3	411.8 – 412	161.6 – 161.8	Mazōn–Montijo *et al.*, 2010
ED	405.2	412	162	Dharmadasa *et al.*, 1989
RF magnetron	405	412	161	Vemuri *et al.*, 2010

sputtering				
ED	405.6	412.3	162.5	this work

CONCLUSION

Materials characterisation of semiconductors is compulsory before any device fabrication and development. PEC measurement is the first step to employ in order to identify the type of electrical conductivity. The resulting layers are usually studied using a range of relevant techniques for their compositional, morphological and optical properties. Techniques such as XRD, XRF are normally used for composition of the deposited film. Morphology of the surfaces are usually observed using SEM and AFM. To analyse the optical properties of the material layers; Raman, optical absorption and XPS are used.

ACKNOWLEDGMENT

REFERENCES

A. Izgorodi, O. W-Jensen, B. W-Jensen and D. R. MacFarlane, Physical Chemistry Chemical Physics 11, 8532 (2009).

A. Smekal, Naturwissenchaften 43, 873 (1923).

A. T. Hubbard, The Handbook of Surface Imaging and Visualization, CRC Press Ltd., (1995).

B. D. Cullity and S. R. Stock, Elements of X-ray Diffraction 3rd edition, Prentice Hall, Inc. Upper Saddle River, New Jersey, U. S. A., (2001).

C. Kittle , Introduction to Solid State Physics 7th edition, John Willey & Sons Inc., New York, (1996).

C. R. Brundle, C. A. Evans Jr, and S. Wilson, Encyclopaedia of Mater. Charact.: Surfaces, Interfaces and Thin Films, Butterworth-Heinemann Inc. USA, (1992).

C. V. Raman and K. S. Krishnan, Nature 21, 501 (1928).

D G Diso, F Fauzi, O K Echendu, A R Weerasinghe and I M Dharmadasa, Journal of Physics: Conference Series **286,** doi:10.1088/1742-6596/286/1/012040, (2011)

D. A. Mazōn-Montijo, M. Sotēlo-Lerma, L. Podríguez-Fernández and L. Huerta, Appl. Surf. Sci. 256, 4280 (2010).

D. Briggs and M. P. Seah, Practical Surface Analysis, John Wiley, Chichester (1990).

D. G. Diso, G. E. A. Muftah, V. Patel and I. M. Dharmadasa, Journal of The Electrochemical Society 157(6), H647-H651 (2010).

D. G. Diso, PhD Thesis, Sheffield Hallam University, UK (2011).

E. Oh, A. K. Ramdas, N. Samarth, H. Luo and J. K. Furdyna, Physical Review B 47(12), 7288 (1993).

E. Smith and G. Dent, Modern Raman Spectroscopy: A Practical Approach, John Wiley & Sons, Ltd., England, (2005).

G. J. Tolan, PhD Thesis, Sheffield Hallam University, UK (2008).

http://Serc.carleton.edu/research./geochemsheets/technique/XRD.html. Retrieved, September 2015.

http://www.wellesley.spectrophotometer. Retrieved, October 2015.

I. M Dharmadasa, A. P Samantilleke, J. Young and N. B Chaure, Semicond. Sci. Technol. **17,** 1238 (2002).

I. M. Dharmadasa, J. M. Thornton and R. H. Williams, Appl. Phys. Letters 54(2), 137 (1989).

I. M. Dharmadasa, S. M. McGregor, I. Wadswort and C. M. Care, Optical Materials 6,75 (1996).

I. Salaoru, P. A. Buffat, D. Laub, A. Amariel, N. Apetroaei and M. Rusu, J. of Optoelectronics & Adv. Mater. 8(3), 939 (2006).

J. F. Moulder, J. Chastain, R. C. King, in: Handbook of X-Ray Photoelectron Spectroscopy: A Reference Book of Standard Spectra for identification and Interpretation of XPS Data, Physical Electronics, Eden prairie, MN, (1995).

K. Ersching, C. E. M. Campos, J. C. de Lima, T. A. Grandi, S. M. Souza, D. L. de Silva and P. S. Pizani, J. of Appl. Phys. 105, 123532 (2009).

K. Siegbahn, Alpha- Beta- and Gamma-Ray Spectroscopy, North-Holland, Amsterdam, (1965).

Kariper A., Güneri E., Göde F. and Gümüs C., Chalcogenide Letters 9(1), 27 (2012).

M. Karimi, M. Rabiee, F. Moztarzadeh, M. Tahriri and M. Bodaghi, Current Appl. Phys. 9, 1263 (2009).

P. M. Martin, Handbook of Deposition Techniques 3rd edition, Elsevier Sci. & Technol., USA, (2010).

Patil S. S. and Pawar P. H., J. Chem. Bio. Physical Sci. 2(2), 968 (2012).

R. Aliyu, D. G. Diso, H. S. Aliyu and L. Grema, African Journal of Physical Sciences 6(3), 23 (2013).

R. F. Egerton, Physical Principles of Electron Microscopy: An Introduction to TEM, SEM and AFM, Springer Science+Business Media, Inc. (2005).

R. S. Vemuri, S. K. Gullapalli, D. Zubia, J. C. McChure and C. V. Ramana, Chemical Physics Letters 495, 232 (2010).

S. M. Sze and Ng. K. Kwok, Physics of Semiconductor Devices 3rd Edition, Wiley-Interscience, (2007).

S. Oktik, Prog. Crystal Growth Charact. **17**, 171 (1989).

S-Y Yang, J-C Chou and H-Y Ueng, Thin Solid Films (2009), doi:10.1016/j.tsf.2009.12.077.

S-Y Yang, J-C Chou and H-Y Ueng, Thin Solid Films **518**, 4197 (2010).

V. Wiedemeier, G. Berth, A. Zrenner, E. M. Larramendi, U. Woggon, K. Lischka and D. Schikora, Semicond. Sci. Technol. 26, 105023 (2011).

W. Szuskiewicz, J. F. Morhange, E. Janik, W. Zaleszczyk, G. Karczewski and T. Wojtowicz, Phys. Status Solidi C 6(9), 2047 (2009).

Reference to this paper should be made as follows: D. G. Diso and A. O. Musa (2015), Review of Basics Material Characterisation of II-VI Thin Film Semiconductors for Use in Solar Cell Fabrication. *J. of Physical Science and Innovation,* Vol. 7, No. 1, Pp. 37-55.

Biographical Notes

D G Diso Obtained a BSc (hons) in Physics from Usman Danfodio University, Sokoto; MSc Physics from Bayero University, Kano and a PhD in Material Science and Solar Energy from Sheffield Hallam University, United Kingdom. Currently working with Kano University of Science & Technology, Wudil, Kano-Nigeria.

A O Musa He is a professor in Physics (Material Science), Obtained a PhD from University of Ilorin and carry out bench work at Newcastle Upon Tyne, United Kingdom. Currently working with Bayero University, Kano-Nigeria.